POLITECNICO DI TORINO
Repository ISTITUZIONALE

On the relevance of facesheet orifice geometry to acoustic liner impedance

Original
On the relevance of facesheet orifice geometry to acoustic liner impedance / Avallone, F., Khedr, A., Paduano, A., Scarano, F., Meirelles, L., Cordioli, J.. - In: NPJ ACOUSTICS. - ISSN 3005-141X. - 2:(2026). [10.1038/s44384-026-00044-x]

Availability:
This version is available at: 11583/3007712 since: 2026-02-17T10:54:15Z

Publisher:
Springer - Nature

Published
DOI:10.1038/s44384-026-00044-x

Terms of use:

This article is made available under terms and conditions as specified in the corresponding bibliographic description in the repository

Publisher copyright

(Article begins on next page)

06 November 2026

npj | acoustics

Article

https://doi.org/10.1038/s44384-026-00044-x

On the relevance of facesheet orifice geometry to acoustic liner impedance

Check for updates

Francesco Avallone[1] ✉, Amr Khedr[1], Angelo Paduano[1], Francesco Scarano[1], Lucas Meirelles[2] & Julio Cordioli[2]

The impact of minor manufacturing deviations in facesheet orifice geometries on the acoustic impedance of liners is studied. Using the lattice-Boltzmann method, simulations of a normal impedance tube (NIT) with plane acoustic waves at sound pressure levels of 130 and 145 dB and frequencies of 800, 1400, and 2000 Hz were performed. Experimental validation was conducted at the Federal University of Santa Catarina using a baseline geometry obtained via 3D scanning and characterized by rounded orifice edges. This geometry was modified to investigate the influence of various edge configurations: sharp edges, double chamfers, and single top chamfers. Results show that sharp-edged orifices increase acoustic resistance and absorption, while geometries with rounded or chamfered edges reduce resistance by up to 28% and lower the absorption coefficient. This is similar to what was found experimentally by performing NIT measurements over different parts of the liner sample. Velocity field analysis reveals that flow separation at the orifice edge is the primary mechanism driving impedance variation, independent of frequency or sound pressure level. These findings underscore the significant influence of small geometric imperfections, often introduced during manufacturing, on liner performance, highlighting the need to consider such variations in industrial design and quality assurance processes.

The reduction of fan noise in turbofan engines remains a central focus in aeroacoustic research, driven by increasingly stringent noise regulations and the demand for quieter aircraft. Among the most effective passive noise control technologies are acoustic liners, which are widely employed in engine nacelles to attenuate tonal and broadband noise generated by the fan stage[1]. These liners typically comprise a perforated facesheet, a honeycomb core, and a rigid backing, forming a resonant structure that dissipates acoustic energy through a combination of viscous, thermal, and reactive mechanisms[2]. The perforated facesheet facilitates energy dissipation via boundary layer interactions at the orifice walls, while the backing cavity enables destructive interference, particularly effective near the blade passing frequency (BPF) during takeoff and landing conditions[3].

A critical parameter influencing liner performance is the geometry of the perforations in the facesheet[4,5]. Recent advancements in liner design have focused on optimizing orifice shape to enhance acoustic absorption, particularly under high-intensity sound fields and complex flow environments[6]. Additive manufacturing has enabled the development of novel Helmholtz resonator (HR) configurations, including extended necks[7], inserted necks[8], spiral necks[9], and tapered necks[10]. These innovations allow for reduced liner thickness without compromising acoustic performance, underscoring the importance of precise geometric control in liner design.

However, the small scale of these perforations presents significant manufacturing challenges[11]. Even minor deviations, such as edge rounding or chamfering, can alter the acoustic-induced flow field and, consequently, the acoustic impedance of the liner[12–15]. In ongoing experimental investigations conducted by the present research group, it was observed that the finish of the orifice edges—whether filleted, chamfered, or sharp—has a measurable impact on acoustic performance. As a matter of fact, variations up to 30% of the measured components of impedance are found when performing normal impedance tube measurements at different locations of the same liner sample. This is because the geometry of the facesheet is not the same for the entire sample[12]. For instance, 3D-printed liners often exhibit filleted edges due to the layer-by-layer deposition process, whereas machined metal liners may feature chamfered or sharp edges depending on the tooling precision. These subtle geometric differences can influence flow separation, vortex shedding, and energy dissipation mechanisms, thereby affecting the overall acoustic response. When compared with porous materials for sound absorption, the impact of manufacturing uncertainty appears to

[1]Department of Mechanical and Aerospace Engineering, Politecnico di Torino, Torino, Italy. [2]Department of Meachanical Engineering, Federal University of Santa Catarina, Florianapolis, Santa Catarina, Brazil. ✉e-mail: francesco.avallone@polito.it

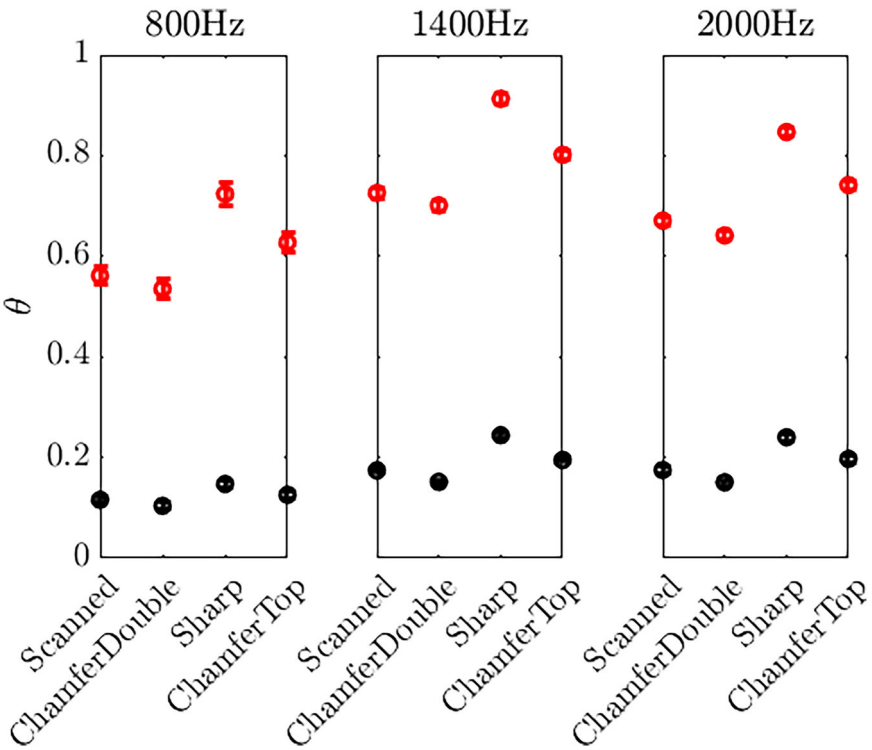

Fig. 1 | Comparison between geometries of the resistance component of impedance. Simulations were performed with acoustic plane waves with different frequencies and amplitudes equal to 130 dB (black) and 145 dB (red).

be higher for cavity-based metamaterials. In fact, using similar normal impedance tube measurements, variations of up to 10% were found for porous material acoustic absorbers[16].

Motivated by these observations, the present study aims to numerically investigate the influence of small variations in orifice edge geometry on the acoustic performance of liners. Computational fluid dynamics (CFD) simulations based on the lattice-Boltzmann (LB) method are employed to isolate the effects of edge shape under normal incidence plane wave excitation, in the absence of grazing flow. Simulations of a normal impedance Kundt tube are conducted at sound pressure levels (SPL) of 130 dB and 145 dB, and at frequencies of 800 Hz, 1400 Hz, and 2000 Hz, to evaluate the sensitivity of acoustic impedance and absorption to edge geometry. The findings provide insights into the role of manufacturing tolerances in liner performance and highlight the need for precise geometric control in both experimental and industrial applications.

Results

Acoustic

Acoustic results are presented in Figs. 1,2, and 3, where resistance and reactance components of impedance and the absorption coefficient are shown. The error bars indicate the maximum and minimum values computed using different pairs of virtual probes.

The analysis highlights the influence of the facesheet orifice geometry on the computed impedance components and absorption coefficients. It is observed that resistance and reactance, as well as the absorption coefficient, vary with the orifice geometry. Specifically, the scanned and double chamfer geometries exhibit the lowest resistance, reactance, and absorption, with minimal differences between them. If one edge is sharpened, as in the chamfer top geometry, resistance, reactance, and absorption increase, and they reach their highest values when both sides are sharpened, i.e., the sharp geometry, for all the frequencies and SPLs. The differences in resistance will be explained in the following by looking at the aerodynamic flow field. The differences in reactance, which are usually linked to the cavity height, can be caused by a different effective length correction for the four geometries[17].

The maximum mass flow rate across the entire sample, during both the inflow and outflow phases, is presented in Fig. 4 for all the test cases. There are differences between the inflow and outflow phases, with the outflow one being smaller by up 20% with respect to the inflow one, unlike what is found in grazing acoustic wave cases[18]. It is observed that the trend of the in- and out-mass flow rate is the opposite of that seen in the acoustic impedance and absorption results. Specifically, the scanned and double chamfer geometries exhibit the highest mass flow rates, with minimal differences. When one edge is sharpened, as in the chamfer top geometry, the mass flow rate decreases, reaching its lowest values for the sharp geometry across all frequencies and SPLs. This inverse relationship occurs because, for the NIT setup, higher acoustic resistance results in a reduction of mass flow. The sharp geometry, which maximizes acoustic impedance and absorption in the case of plane waves, presents the lowest mass flow rate, while the less sharp ones present the highest. This suggests that the boundary layer forming over the orifice walls plays a relevant role even when the liner operates in the linear regime.

Figure 5 presents the quality factor Q. The results indicate that, for most cases, Q follows a similar trend to the impedance, increasing as the orifice edges become sharper. This behavior is consistent with the theoretical relationship between Q and acoustic resistance, where a higher resistance leads to lower damping and thus a higher Q factor[19]. The scanned and double chamfer geometries exhibit the lowest Q values, suggesting greater energy dissipation. Conversely, the chamfer top and sharp geometries yield the highest Q, indicating reduced dissipation. It is worth mentioning that, in this study, the parameter τ^* was considered to be constant and only the quality factor was optimized. However, the end correction terms in τ^* might also be affected by the orifice geometry.

Flow-field

All the trends described above are influenced by the vena-contracta effect, which alters the effective orifice area and modifies the in-orifice velocity dynamics[19]. To this end, the vertical velocity profiles, perpendicular to the facesheet, nondimensionalized by the speed of sound in air (a_∞), within the orifice at the midplane of the facesheet during the inflow and outflow phases are shown in Fig. 6 for all SPL and frequency values. Each subfigure presents the velocity profiles for the four geometries, extracted in the middle of the facesheet thickness. The spanwise location

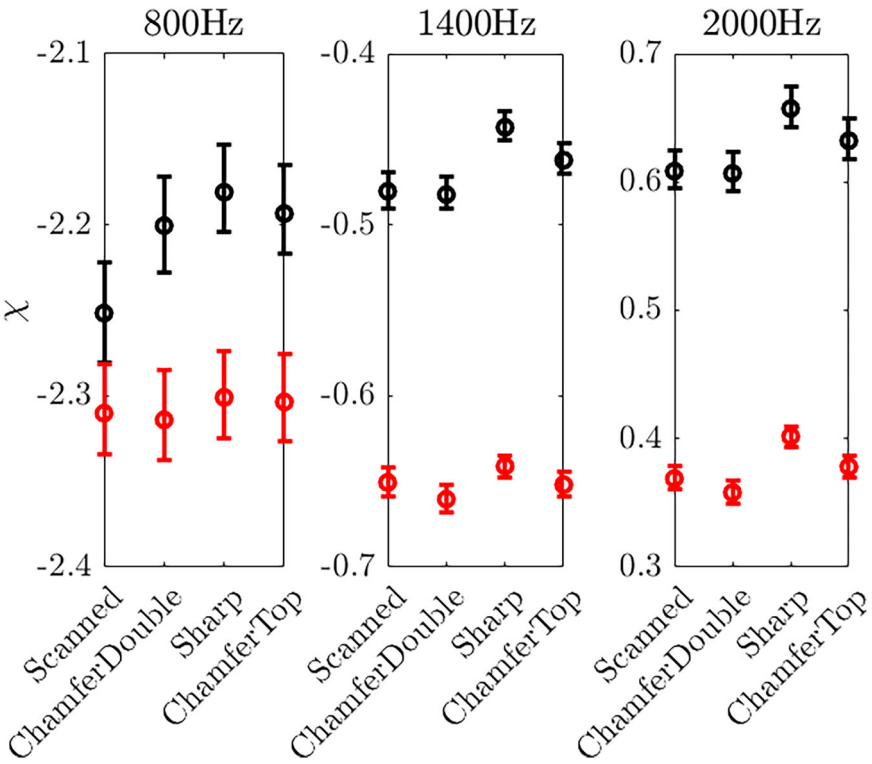

Fig. 2 | Comparison between geometries of the reactance component of impedance. Simulations were performed with acoustic plane waves with different frequencies and amplitudes equal to 130 dB (black) and 145 dB (red).

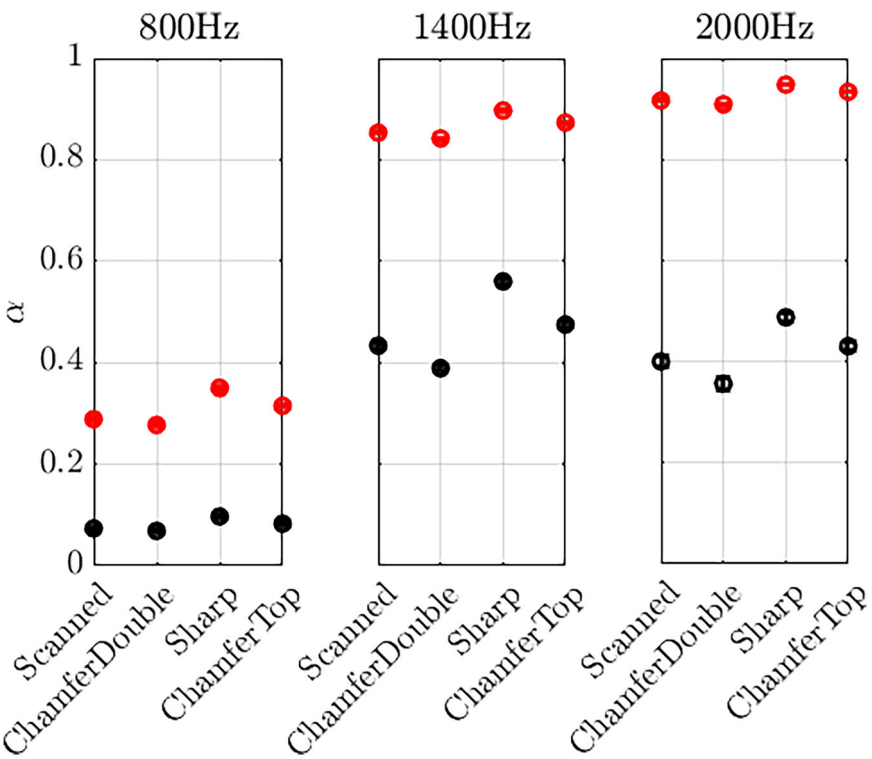

Fig. 3 | Comparison between geometries of the absorption coefficient. Simulations were performed with acoustic plane waves with different frequencies and amplitudes equal to 130 dB (black) and 145 dB (red).

corresponds to the plane crossing two orifices in the streamwise direction (refer to Fig. 9). Notably, at 1400 Hz, the vertical velocities during both inflow and outflow phases exhibit the highest values. For SPL = 130 dB, the peak velocity is significantly lower, approximately five times smaller than that at SPL = 145 dB.

Comparing the different geometries, the sharp-edged orifice consistently exhibits the highest inflow velocities across nearly all SPL and frequency combinations. Conversely, the scanned and double chamfer geometries display similar velocity profiles, both during the inflow and outflow phases, due to their comparable edge designs. The chamfer top geometry shows intermediate inflow velocities; however, during the outflow phase, it occasionally surpasses the sharp geometry in velocity magnitude. This velocity profile trend aligns with impedance and mass flow results (Figs. 1–4). Sharp geometries, with the highest acoustic

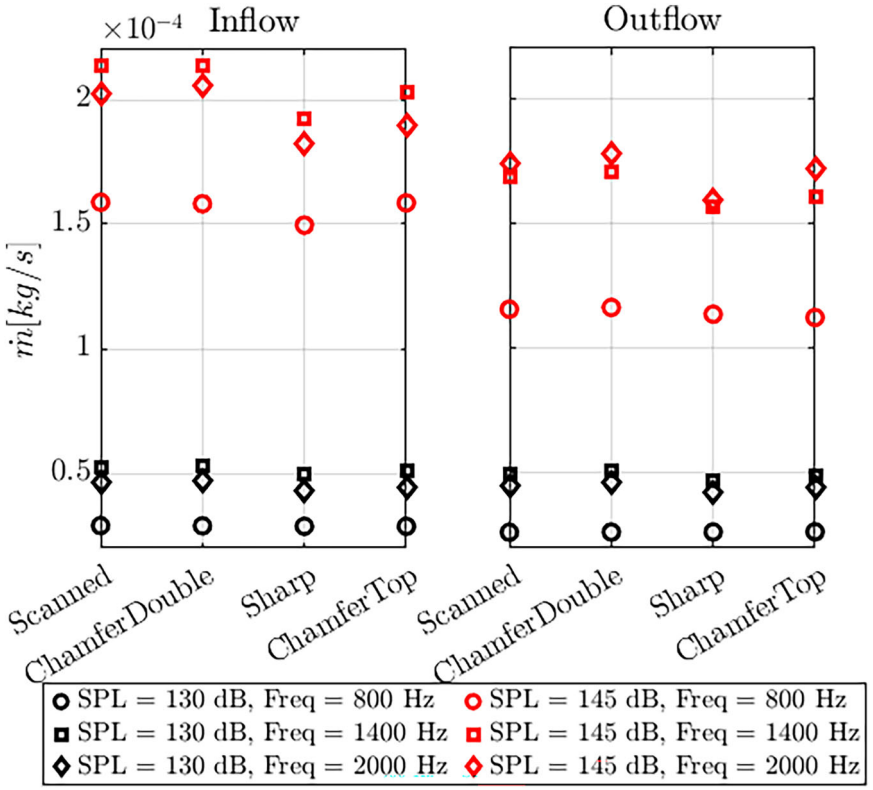

Fig. 4 | Comparison between geometries of the mass flow. Simulations were performed with acoustic plane waves with different frequencies and amplitudes equal to 130 dB (black) and 145 dB (red).

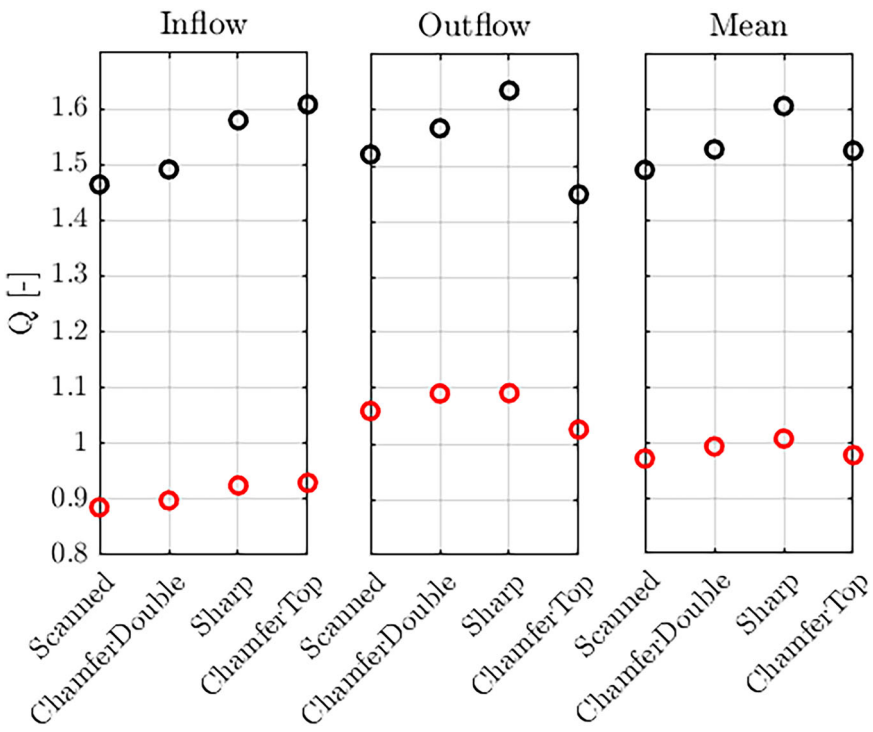

Fig. 5 | Comparison between geometries of the quality factor. Simulations were performed with acoustic plane waves with different frequencies and amplitudes equal to 130 dB (black) and 145 dB (red).

resistance and absorption, generate intense localized inflow velocities, due to the vena contracta effect, also visible in the vertical velocity contours in Fig. 7 (1st and 2nd rows). These contours are obtained through phase-averaging. It was applied by aligning signals to a common phase reference and computing the ensemble mean over repeated cycles. This isolates deterministic periodic behavior while suppressing cycle-to-cycle fluctuations. The figure highlights the pronounced recirculation for the sharp edge. As a matter of fact, at both side edges, the flow recirculates and detaches from the facesheet walls more than in the other cases. As a consequence, the effective cross-sectional flow area reduces, thus resulting in the lowest net mass flow. Scanned and double-chamfered geometries reduce flow contraction through symmetric edge

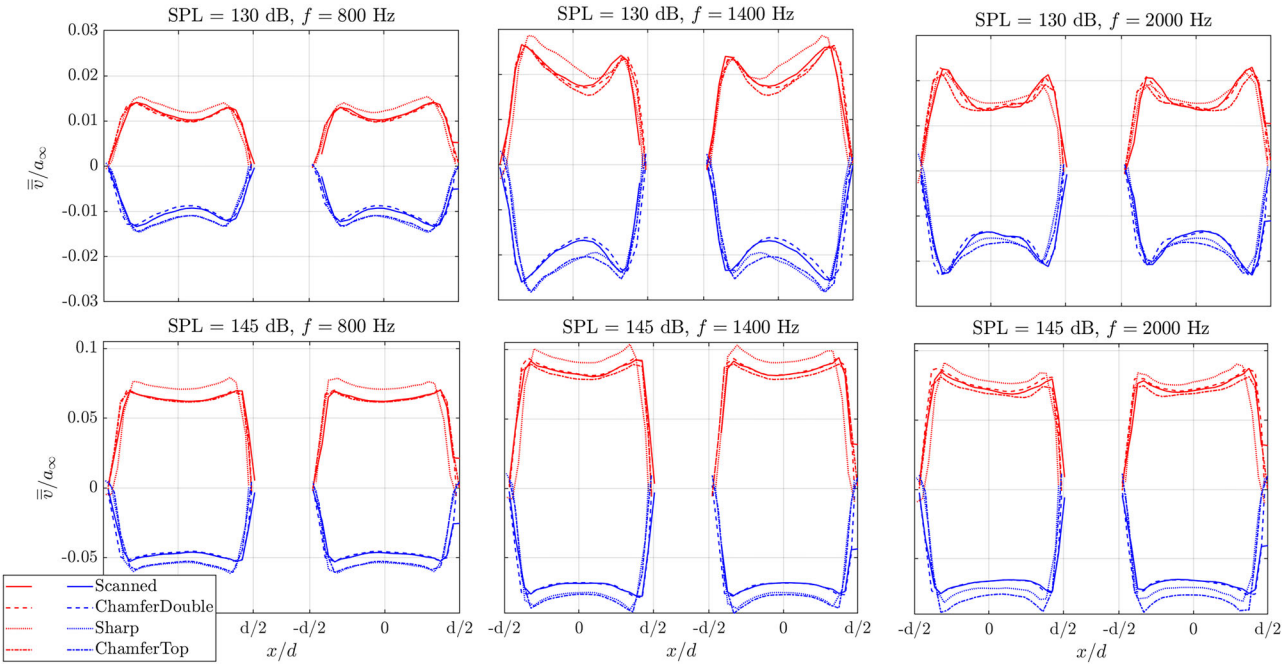

Fig. 6 | Phase-averaged velocity profiles at the center of the facesheet for different geometries. The inflow is shown in red, while the outflow phase is in blue.

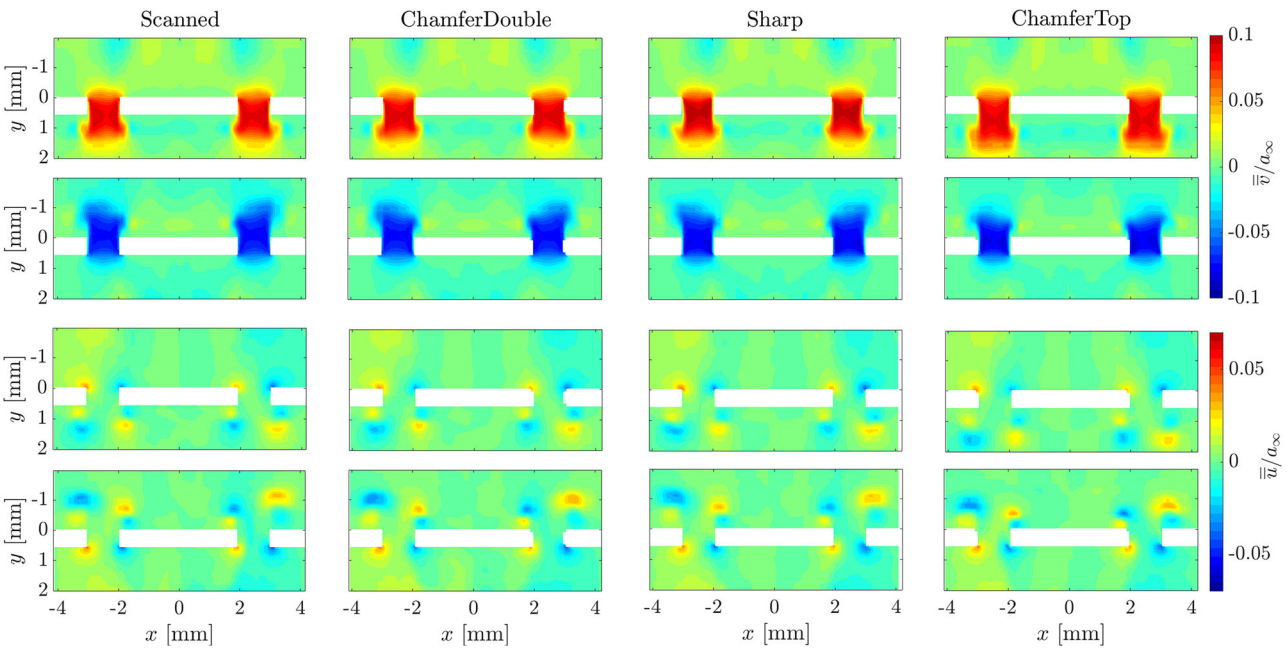

Fig. 7 | Comparison between geometries of the phase-averaged velocity contours. The vertical velocity is reported in the 1st and 2nd rows, while the horizontal velocity is shown in the 3rd and 4th rows. The inflow phase is shown in the 1st and 3rd rows, and the outflow in the 2nd and 4th rows. Results are plotted for a plane acoustic wave with an amplitude equal to 145 dB and a frequency of 1400 Hz.

treatments, lowering resistance and enabling higher mass flow despite diminished peak velocities. The chamfered top geometry balances these effects: its chamfered inflow edge mitigates separation, reducing resistance compared to the sharp case, while the sharp outflow edge increases expulsion resistance. This asymmetry explains why the chamfer top geometry achieves intermediate absorption (Fig. 3) and occasionally exceeds the sharp geometry in outflow velocity acceleration. However, its overall mass flow remains lower than the scanned and double-chamfered cases due to residual outflow losses. These mechanisms scale consistently with SPL, reflecting acoustic forcing intensity.

It is interesting to notice that the velocity profiles, for all the cases, are not symmetric within the orifice, thus suggesting that there is a fluid dynamic interaction between the orifices, even at the lowest SPL analyzed. The horizontal velocity contours (Fig. 7, 3rd & 4th rows) further clarify these dynamics. During the inflow (3rd row), sharp geometries exhibit larger recirculation zones that restrict mass flow. During the outflow (4th row), the sharp geometry's horizontal velocity field reveals a narrow, high-speed jet, whereas the scanned and double-chamfered geometries produce broader, slower jets. Chamfer top's outflow (4th row) combines features of both: its sharp bottom edge generates a jet, while the chamfered top edge from the

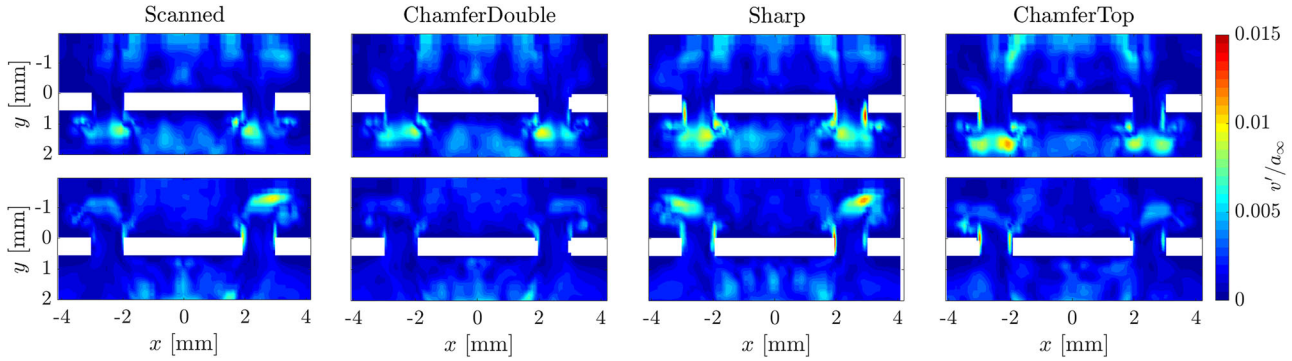

Fig. 8 | Comparison between geometries of the RMS contours of the vertical velocity. The inflow phase is shown in the 1st row, while the outflow is in the 2nd row. Results are plotted for a plane acoustic wave with an amplitude equal to 145 dB and a frequency of 1400 Hz.

inflow phase minimally perturbs the expelled flow, explaining its intermediate mass flow and occasional velocity exceedance.

Figure 8 illustrates the root-mean-square (RMS) contours of vertical velocity fluctuations during the inflow and outflow phases at 145 dB and 1400 Hz. During the inflow (1st row), the sharp-edged orifice exhibits the highest RMS values near the orifice walls, consistent with intense turbulent shear layers generated by abrupt flow contraction and vena contracta effects. The chamfer top geometry shows moderately high RMS levels at the orifice walls, but the highest fluctuations inside the cavity, likely due to asymmetric vorticity generation from its chamfered inflow edge interacting with the sharp outflow edge. In contrast, scanned and double-chamfered geometries display minimal RMS amplitude at the walls and low fluctuations within the cavity, reflecting their smoother inflow patterns and reduced flow separation. During the outflow (2nd row), the sharp geometry produces the strongest RMS fluctuations outside the orifice, indicative of turbulent jet expulsion, while the chamfer top shows elevated wall-adjacent fluctuations. Scanned and double-chamfered cases maintain low RMS values at both locations. Asymmetry in the RMS contours across all geometries emphasizes the three-dimensional nature of vortex shedding and turbulence.

Discussion

This work systematically evaluates the influence of orifice edge geometry on the performance of single-degree-of-freedom acoustic liners through high-fidelity lattice-Boltzmann very-large-eddy simulations. Four face-sheet orifice geometries with the same inner diameters have been generated; they have been conceived to reproduce possible manufacturing uncertainties with additive manufacturing, based on the author's experience. An ideal facesheet with sharp edges has been modified by rounding the edge or by making the edge chamfered. By analyzing the four configurations in a Kundt tube numerical experiment, i.e., in the absence of either a grazing or bias flow under varying sound pressure levels and frequencies, key insights into the interplay between edge geometry, acoustic impedance, and flow dynamics are established. The sharp-edged orifice increases acoustic resistance and absorption. In contrast, unsharpened edges (scanned and double-chamfered geometries) reduce acoustic absorption because they increase the mass flow rates within the orifices. By introducing a chamfered or round edge, thus changing the outer orifice diameter by 10% with respect to the sharp orifice diameter, an increase up to 28% of resistance is found. RMS velocity fluctuations highlight the role of edge geometry in vortex generation, as the sharp edges produce intense shear layers.

These findings emphasize that manufacturing imperfections—often dismissed in idealized models—critically influence liner performance. For industries relying on perforated liners, this study underscores the importance of stringent quality control to minimize geometric deviations and calibrate predictive tools to account for real-world imperfections. Similarly, it is recommended to perform scans of the geometries when comparing results carried out within the context of benchmarking activities to allow a fair comparison.

Methods

Flow solver

The commercial software 3DS Simulia PowerFLOW 6, in its high-subsonic version, i.e., up to a Mach number of 0.9, is used to compute the transient flow field. The solver has already been validated in the past for canonical honeycomb liner configurations, both in the absence of flow[20–22] and with grazing flow[23,24]. The same solver has also been used to simulate the effect of a single-degree-of-freedom (SDOF) liner installed on the nacelle of the NASA Source Diagnostic Test engine configuration[25], and the predicted sound attenuation has been recently confirmed by another simulation carried out by using a different high-fidelity flow solver[26].

PowerFLOW flow simulation technology is based on an LB method with collision relaxation time and distribution function dynamically calibrated to the time scales of slow turbulent structures, modelled through a turbulence transport model. Some of the key properties of the model are described in the following paragraphs.

The LB scheme is based on an expansion of the distribution function $f(\mathbf{x}, \boldsymbol{\xi}, t)$, say the probability density of finding particles at location $\mathbf{x}$, advected at velocity $\boldsymbol{\xi}$ at time t, solution of the Boltzmann equation, in a series of Hermite polynomials[27]. These constitute an orthogonal basis, which is particularly suited to describe a flow in the kinetic space. Indeed, the first four coefficients, from 0^{th} to 3^{rd} order, of the expansion of the Maxwellian distribution function $f^{(0)}$ at equilibrium are algebraically related to the moments of macroscopic flow, say mass, momentum, energy/momentum fluxes, and heat fluxes. An interesting property of a Hermite expansion is that the series can be truncated at a given order without altering the low-order coefficients; therefore, an expansion of f truncated at the order $N > 3$ provides a unique representation of the macroscopic hydrodynamic status of a fluid.

A key component of PowerFLOW LB scheme is the usage of a regularized collision operator Ω_i in the non-dimensional lattice Boltzmann equation $f_i(\mathbf{x} + \boldsymbol{\xi}_i, t + 1) = f_i(\mathbf{x}, t) + \Omega_i$ projected along the discrete particle velocity $\boldsymbol{\xi}_i$. Following[28], the LB equation can be equivalently written as $f_i(\mathbf{x} + \boldsymbol{\xi}_i, t + 1) = f_i^{(0)}(\mathbf{x}, t) + f_i^{(1)}(\mathbf{x}, t) + \Omega_i$, where $f_i^{(1)}$ is the perturbation. In conditions that are not very far from equilibrium, the collision operator is linearly related to the the perturbation through coefficients that are negatively/inversely proportional to relaxation time τ_{ij} of the collision process along the discrete velocity direction i due to chaotic motion along the direction j, say $f_i(\mathbf{x} + \boldsymbol{\xi}_i, t + 1) = f_i^{(0)}(\mathbf{x}, t) + \sum_j \delta_{ij} - 1/\tau_{ij} f_i^{(1)}(\mathbf{x}, t)$. If the perturbation is expanded in a Hermite series, this starts with the second-order term and can be truncated at the third-order term to recover the macroscopic fluid status. The resulting regularized collision operator will therefore include only terms proportional to the second-order Hermite polynomials, accounting for energy and momentum fluxes, and third-order terms, accounting for heat fluxes. Finally, following[29], applying Galilean invariance to the collision operator results in a two-term regularized form, in which the two terms account for energy/momentum fluxes and

Table 1 | Environmental conditions during experiments

Ambient pressure	1020.53 hPa
Temperature	23.30 °C
Relative Humidity	50.2 %
Estimated Air Density	1.197 kg m^{-3}
Estimated Speed of Sound	345.95 m s^{-1}

heat fluxes, respectively, with corresponding relaxation times related to the macroscopic fluid viscosity and thermal conductivity.

Another important component of the present flow simulation methodology is related to turbulence modeling, which is key to tackling high Reynolds number flows. The way turbulence is accounted for in PowerFLOW is by modifying the relaxation time in the collision operator by considering the time scales related to the turbulent motion and to the strain rate and rotation of the resolved flow field. Moreover, the amount of turbulent kinetic energy is used to define the equilibrium state of the gas. Such a procedure is based on the paradigm of a kinetic theory applied to a "gas of eddies" and it can be interpreted as an expanded analogy between the chaotic motion of particles (and the internal energy) and the chaotic motion of eddies (and the turbulent kinetic energy), which is indeed the essence of the Boussinesq analogy. As discussed by[30], the expansion of the kinetic theory from particles to eddies leads to the fundamental observation that the Reynolds stresses, which are a consequence of the chaotic turbulent motion, have a non-linear structure and are better suited to represent turbulence in a state far from equilibrium, as in the presence of distortion, shear, and rotation. In other words, although the relaxation time is computed using a two-equation transport model, the k-ϵ Re-Normalization Group (RNG) model in PowerFLOW[31,32], this is not used to compute an equivalent eddy viscosity, like in Reynolds-Averaged Navier Stokes (RANS) models, but it is instead used to dynamically recalibrate the Boltzmann model to the characteristic time scales of a turbulent flow motion. Hence, no Reynolds stresses are explicitly added to the governing equations, and those are an implicit consequence of the chaotic exchange of momentum driven by the turbulent flow with characteristic times smaller than the slowly-varying turbulent flow. The underlying concept of a dynamic gas system continuously driven towards equilibrium as a consequence of an intimate coupling between the LB kinetic model and the turbulence transport model is the essence of the LB/VLES hybrid approach.

The LB/VLES equations are solved on a Cartesian mesh, which is automatically generated for any complex shape of the boundary conditions. Variable Resolution (VR) regions can be defined in the flow domain to locally refine the grid size by successive factors of 2. By construction, in a time step, particles are advected exactly from one point to the other points of the lattice stencils. Therefore, the local time step varies by a factor of 2 in adjacent VRs. Bounce-back boundary conditions for no-slip walls and the specular reflection for frictionless walls are ensured thanks to a generalized volumetric formulation for the intersection of arbitrary-oriented surface elements and the volume elements[33]. Finally, a wall model accounting for pressure gradients is used to model boundary layer behaviours at high Reynolds numbers[32].

Experimental setup

Experimental data were obtained with a Brüel&Kjær (B&K) Portable Impedance Meter System, Type 9737. The system was connected to a B&K LAN-XI, type 3160-A-042, for signal acquisition, integrated with the driver signal amplifier, type WB-3592. Built-in temperature, ambient pressure, and humidity sensors register the measurement conditions and update derived variables, such as the speed of sound. This system has been used previously in various investigations[34–36].

An acoustic field was generated by an integrated 50 W driver, which is capable of providing up to 150 dB OASPL. Acoustic pressure was measured by two pressure-field 1/4" B&K microphones, type 4187, with type 2670-W-012 pre-amplifiers. In the assembly, the microphones are positioned approximately 20 mm apart, flush-mounted on the inner wall of the tube. Such microphone spacing ensures higher accuracy for measuring frequencies higher than 850 Hz, approximately, according to the ISO 10534-2. The waveguide is a 208.2 mm long B&K WA-1599-W-070 tube, with a 29 mm inner diameter. Its dimension satisfies only plane wave propagation criteria for frequencies up to 5.9 kHz[37]. Therefore, the system can provide impedance results for frequencies between 850 Hz and 5.9 kHz with satisfying accuracy.

The measurements were preceded by a calibration procedure to obtain the ISO 'predetermined calibration factor' H_C, relating the transfer functions between the two microphones. Additionally, the acoustic center of both microphones was determined. Both procedures followed ISO standardized steps. Environmental conditions during experimental procedures are given in Table 1.

Impedance, absorption coefficient and quality factor

In both experiments and computations, impedance Z was determined from the reflection coefficient r[38]:

$$\frac{Z}{\rho c_0} = \frac{1+r}{1-r}, \tag{1}$$

where ρ is the air density and c_0 is the speed of sound. The reflection coefficient was determined from the transfer functions between the microphone signals:

$$r = \frac{H_{12} - H_I}{H_R - H_{12}} e^{2jk_0 x_1}, \tag{2}$$

where j is the imaginary unit, $k_0 = \omega/c_0$ is the free-field wavenumber ($\omega = 2\pi f$ being the angular frequency of the excited acoustic field with frequency f) and x_1 is the distance between the sample and the furthest microphone. In Equation (2), H_{12} is the measured transfer function (TF) corrected with H_C, while H_R and H_I are the real and imaginary parts, respectively, of the uncorrected H_{12}.

The absorption coefficient was obtained as:

$$\alpha = 1 - r. \tag{3}$$

During the experimental measurements, it was ensured that no gap existed between the tube's free end and the sample. Air leakage was prevented using a thin rubber seal, glued to the free end of the tube. The seal was already present during the calibration procedures.

Numerical data were also used to compute the quality factor Q, computed by optimizing the fit between the theoretical[39], adopted in previous studies[18,19], and simulated vertical acoustical velocity $\overline{\overline{v}}$ across the analyzed frequencies (800, 1400, and 2000 Hz). The theoretical acoustical velocity is given by[39]:

$$\overline{\overline{v}} = \frac{p'}{\rho_0 \omega \tau^*} \frac{1}{\sqrt{\left[\left(\frac{\omega_0}{\omega}\right)^2 - 1\right]^2 + \left(\frac{\omega_0}{\omega Q}\right)^2}}. \tag{4}$$

where p' is the root mean square of the pressure obtained from the SPL, ω_0 is the fundamental resonance frequency, ω is the plane wave frequency, $\tau^*$is the sum of the geometrical neck thickness τ and $0.8d$, where d is the orifice diameter and Q is the quality factor, which exact value is not precisely know[19].

Computational setup and validation

The liner geometry consists of 33 cells, each featuring a facesheet with eight orifices positioned over a rectangular cavity, as illustrated in Fig.

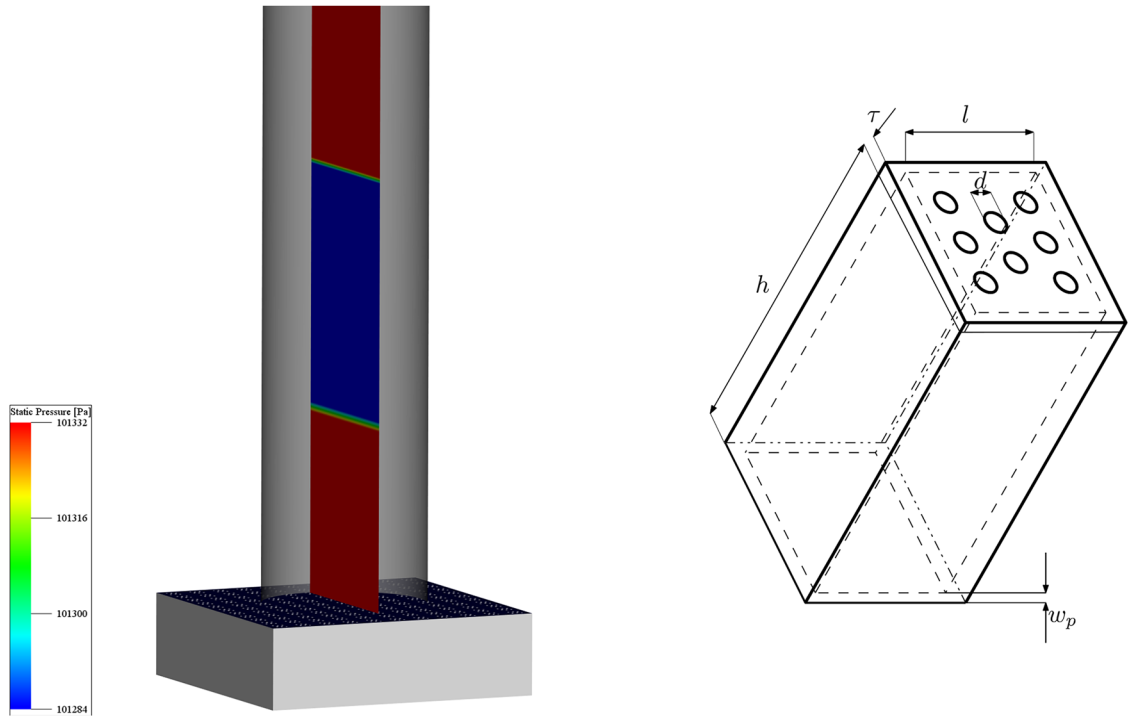

Fig. 9 | Schematic of the computational domain. The acoustic wave propagating from the top to the bottom is shown on the left. The geometry of the liner with reference dimensions is shown on the right.

Fig. 10 | Liner facesheet geometries tested with the normal impedance tube computational setup. Each geometry differs for the orifice finishes.

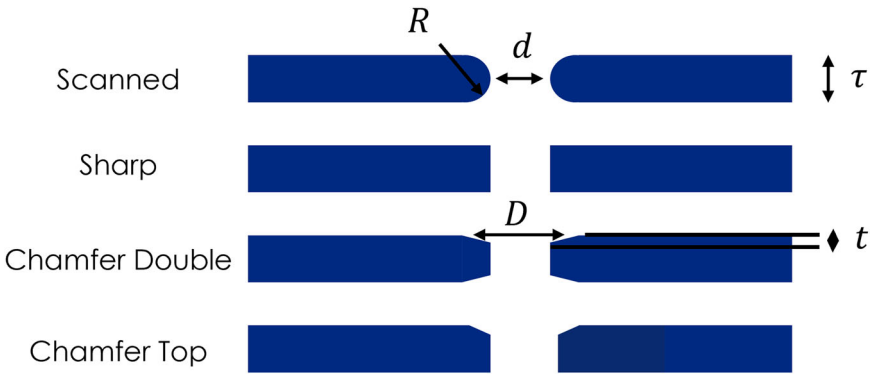

Table 2 | Geometrical parameters of the liners tested with the normal impedance tube setup

τ	d	D	R	t
0.55 mm	1.17 mm	1.29 mm	0.066 mm	0.1 mm

9. The parametric analysis was carried out on four different facesheet orifice geometries, as shown in Fig. 10. These geometries were derived by modifying a reference experimental geometry, named scanned, which was obtained through the 3D scanning of the available geometry[24], considering the manufacturing uncertainty that was detected. In addition to the scanned geometry, three alternative configurations were considered: sharp, chamfer double, and chamfer top. The corresponding geometrical parameters are provided in Table 2. The height of the cavity h is 38.1 mm, and the side of the square cavity l is 9.89 mm. The theoretical resonance frequency of the current acoustic liner geometry is 1170 Hz[40].

The four liner geometries were tested numerically using the commercial software PowerFLOW. A normal impedance tube (NIT) setup was automatically constructed using *OptydB − Kundt*. The NIT setup consists of a tube, positioned above the simulated acoustic liner (Fig. 9, left), whose length varies based on the minimum frequency of interest, set to 50 Hz. For the present case, the duct has a length of 2.28 m and a diameter of 0.08 m. The tube does not cover the entire liner geometry but only a part of it. The flow field is simulated only in the cells covered by the tube.

Acoustic plane waves, in the form of truncated sine waves, are introduced as an initial condition and provided to the software through an input table. The plane waves are not introduced as a time-dependent boundary condition, but as a spatially varying initial condition. To guarantee statistical convergence, at least ten wavelengths at the minimum frequency are simulated. Tonal acoustic plane waves with amplitudes of 130 dB and 145 dB and frequencies of 800, 1400, and 2000 Hz were tested. An example of the spectral content of the input acoustic waves for the two investigated amplitudes at a tonal frequency of 1400 Hz is shown in Fig. 11. The two

amplitudes were selected because they correspond to linear and non-linear operating regimes of SDOF liner[22,41].

The computational domain was discretized using nine VR regions, with a minimum voxel size of 20 vx/τ (0.0274 mm). The grid resolution was highest near the face-sheet orifice and decreased further away. The voxel size doubles from one VR region to the other. It was ensured that the resolution remained above 15 vx per wavelength for the shortest wavelength of interest. The VR regions used to discretize the computational domain are represented in Fig. 12. In the current setup, the minimum and maximum frequencies of interest were set to 50 Hz and 2500 Hz, respectively, resulting in a total simulation time of 0.02 s.

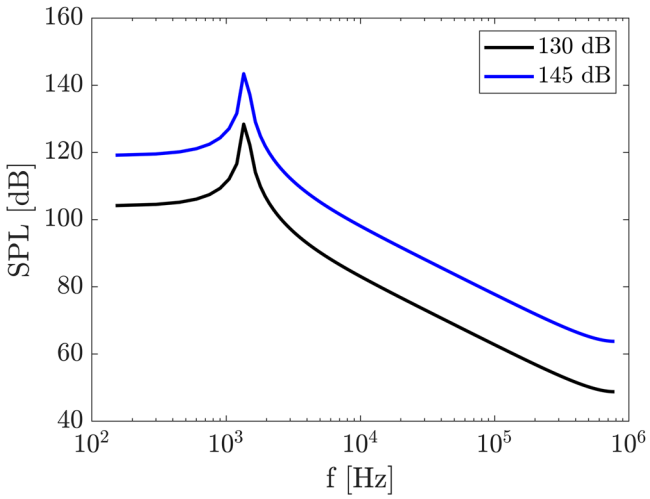

Fig. 11 | Sound pressure level spectra given as input to the normal impedance tube simulations. The black line represents the 130dB acoustic wave, while the blue one represents the 145 dB one.

Data were sampled at a frequency of 50 kHz. Ten virtual probes were placed along the centerline of the duct, evenly spaced between 0.228 m and 1.144 m above the liner. These probes were used to compute impedance, using the two-microphone method approach as in the experiments[38]. From the two-microphone method, the reflection coefficient is measured; then, both the impedance and the absorption coefficient are obtained. In the subsequent analysis, data from the ten probes were averaged, and error bars indicate the minimum and maximum values of the computed impedance and absorption coefficients.

Before conducting simulations for all geometries of interest and plane acoustic waves, a grid resolution study was performed using three different resolutions: 10 vx/τ, 20 vx/τ, and 40 vx/τ. The geometry selected for this study was the scanned configuration, for which experimental results were obtained using the normal impedance tube at the Federal University of Santa Catarina (UFSC), Brazil. The grid resolution study was conducted for a single condition: a tonal acoustic plane wave with an amplitude of 145 dB and a frequency of 1400 Hz due to significant nonlinear effects[22].

Results from the grid resolution study are presented in Fig. 13, alongside experimental data for comparison. Experiments were obtained using a broadband noise excitation with an overall sound pressure level of 145 dB. The error bars indicate the minimum and maximum values obtained by performing experiments on four parts of the same liner sample. From an experimental perspective, it is found that a variation of about 30% is present when measuring impedance with the normal impedance tube by placing it at different locations over the facesheet. This is because the orifice geometry is not the same everywhere[12]. The comparison between experimental and numerical results indicates that the simulations slightly overpredict the experimental resistance θ, while reactance χ values are in closer agreement. This discrepancy may arise from minor differences between the orifice geometries in the numerical simulations and those in the experiments, and differences in the acoustic excitation[42]. The computational results demonstrate a converging trend with increasing grid resolution. A resolution of 20 vx/τ was selected as a suitable compromise between computational accuracy and cost.

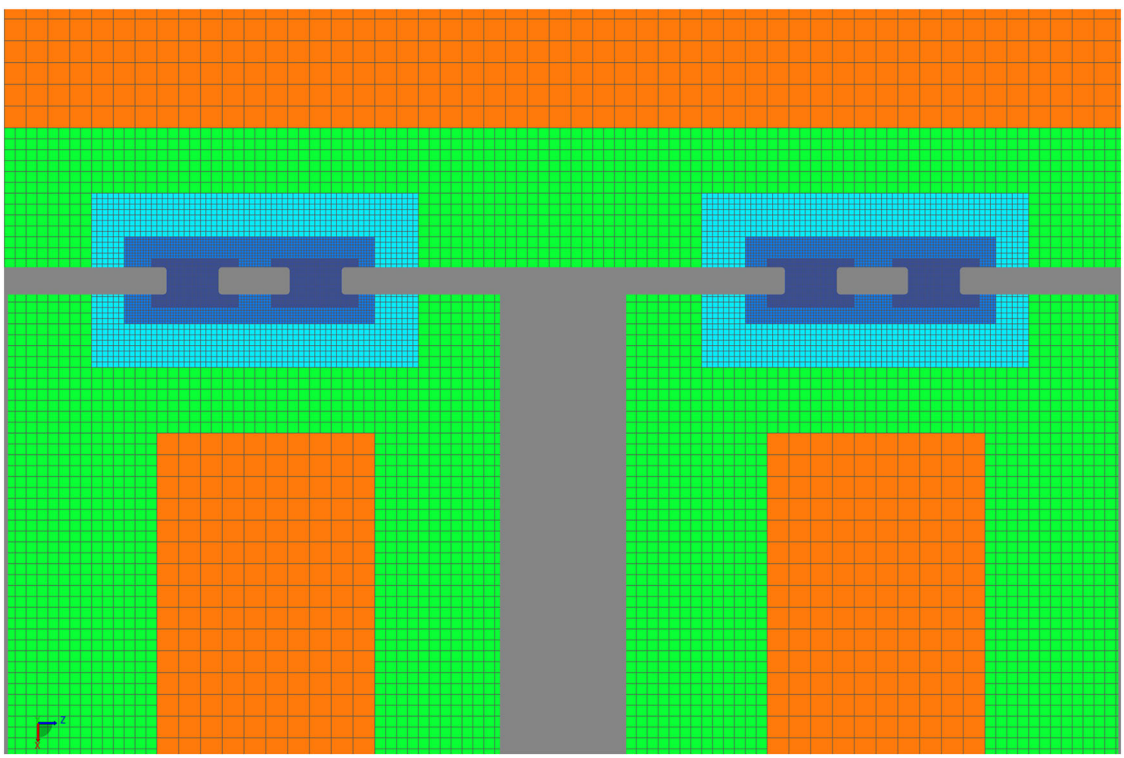

Fig. 12 | Grid adopted to discretize the computational domain. Different colors represent the different variable resolution regions.

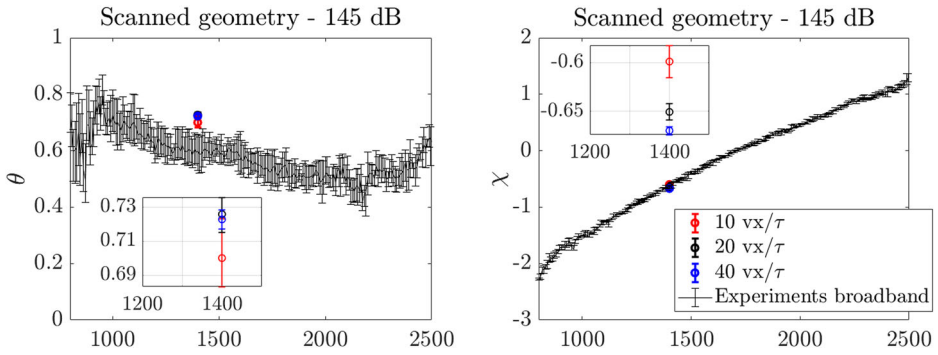

Fig. 13 | Grid resolution study. On the left, the resistance, and on the right, the reactance component of impedance for three different grid resolutions. Symbols represent the numerical results, while the continuous line with the uncertainty bar represents the experimental one.

Data availability

Data are fully available upon request to the authors.

Received: 10 July 2025; Accepted: 13 January 2026;
Published online: 17 February 2026

References

1. Casalino, D., Diozzi, F., Sannino, R. & Paonessa, A. Aircraft noise reduction technologies: a bibliographic review. *Aerosp. Sci. Technol.* **12**, 1–17 (2008).
2. Smith, M. J. *Aircraft Noise*, vol. 3 (Cambridge University Press, 2004).
3. Envia, E. Fan noise reduction: an overview. *Int. J. Aeroacoustics* **1**, 43–64 (2002).
4. Gaeta, R. & Ahuja, K. Effect of orifice shape on acoustic impedance. *Int. J. Aeroacoustics* **15**, 474–495 (2016).
5. Zhao, D., Ji, C. & Wang, B. Geometric shapes effect of in-duct perforated orifices on aeroacoustics damping performances at low Helmholtz and Strouhal number. *J. Acoustical Soc. Am.* **145**, 2126–2173 (2019).
6. Mahesh, K., Ranjith, S. K. & Mini, R. Recent advancements in helmholtz resonator based low-frequency acoustic absorbers: a critical review. *Arch. Comput. Methods Eng.* **31**, 2079–2107 (2024).
7. Selamet, A. & Lee, I. Helmholtz resonator with extended neck. *J. Acoustical Soc. Am.* **113**, 1975–1985 (2003).
8. Huang, S. et al. Acoustic perfect absorbers via Helmholtz resonators with embedded apertures. *J. Acoustical Soc. Am.* **145**, 254–262 (2019).
9. Guo, J., Zhang, X., Fang, Y. & Jiang, Z. A compact low-frequency sound-absorbing metasurface constructed by resonator with embedded spiral neck. *Appl. Phys. Lett.* **117**, (2020).
10. Song, C. et al. Perfect acoustic absorption of Helmholtz resonators via tapered necks. *Appl. Phys. Express* **15**, 084006 (2022).
11. Chojnacki, B., Wojciech Binek, A. C., Pawlik, J. & Idczak, J. Accuracy of 3d printing of the samples in the prototyping of cavity-based metamaterials. *Sci. Rep.* **15**, 13259 (2025).
12. Meireilles, L.*High-Fidelity Numerical Simulations of Acoustic Liners Under Grazing Flow*. Master's thesis, Federal University of Santa Catarina (2023).
13. Fusaro, G. et al. Investigation of the impact of additive manufacturing techniques on the acoustic performance of a coiled-up resonator. *J. Acoustical Soc. Am.* **153**, 2921– (2023).
14. Zieliński, T. G. et al. Reproducibility of sound-absorbing periodic porous materials using additive manufacturing technologies: Round robin study. *Addit. Manuf.* **36**, 101564 (2020).
15. Jamois, A., Dragna, D., Zieliński, T. G. & Galland, M. A. Acoustic absorption of 3d printed samples at normal incidence and as a duct liner. *Acta Acust.* **9**, 12 (2025).
16. Roozen, N. & Piana, E. Uncertainty analysis of acoustic and non-acoustic parameters derived from four-microphone impedance tube measurements. *Appl. Acoustics* **198**, (2022).
17. S., T. *Elements of acoustics* (Wiley, 1981).
18. Zhang, Q. & Bodony, D. J. Numerical investigation of a honeycomb liner grazed by laminar and turbulent boundary layers. *J. Fluid Mech.* **792**, 936–980 (2016).
19. Léon, O., Méry, F., Piot, E. & Conte, C. Near-wall aerodynamic response of an acoustic liner to harmonic excitation with grazing flow. *Exp. fluids* **60**, 1–18 (2019).
20. Mann, A., Perot, F., Kim, M.-S. & Casalino, D. Characterization of acoustic liners absorption using a lattice-Boltzmann method (2013).
21. Hazir, A. & Casalino, D. Effect of temperature variations on the acoustic properties of engine liners (2017).
22. Manjunath, P., Avallone, F., Casalino, D., Ragni, D. & Snellen, M. Characterization of liners using a lattice-Boltzmann solver (2018).
23. Avallone, F., Manjunath, P., Ragni, D. & Casalino, D. Lattice-boltzmann very large eddy simulation of a multi-orifice acoustic liner with turbulent grazing flow (2019).
24. Paduano, A. et al. On the impact of the acoustic wave direction on the in-orifice flow dynamics of an acoustic liner grazed by a turbulent flow (2024).
25. Casalino, D., Hazir, A. & Mann, A. Turbofan Broadband Noise Prediction Using the Lattice Boltzmann Method. *AIAA J.* **56**, 1–20 (2017).
26. Shur, M., Strelets, M., Travin, A., Suzuki, T. & Spalart, P. Unsteady Simulations of Sound Propagation in Turbulent Flow Inside a Lined Duct. *AIAA J.* 1–17 (2021).
27. Shan, X., Yuan, X.-F. & Chen, H. Kinetic theory representation of hydrodynamics: a way beyond the Navier-Stokes equation. *J. Fluid Mech.* **550**, 413–441 (2006).
28. Zhang, R., Shan, X. & Chen, H. Efficient kinetic method for fluid simulation beyond the Navier-Stokes equation. *Phys. Rev. E Stat. Nonlinear Soft Matter Phys.* **74**, 046703 (2006).
29. Chen, H., Gopalakrishnan, P. & Zhang, R. Recovery of Galilean invariance in thermal lattice Boltzmann models for arbitrary Prandtl number. *Int. J. Mod. Phys. C.* **25**, 1450046 (2014).
30. Chen, H., Orszag, S., Staroselsky, I. & Succi, S. Expanded analogy between Boltzmann kinetic theory of fluids and turbulence. *J. Fluid Mech.* **519**, 301–314 (2004).
31. Yakhot, V., Orszag, S., Thangam, S., Gatski, T. & Speziale, C. Development of turbulence models for shear flows by a double expansion technique. *Phys. Fluids A* **4**, 1510–1520 (1992).
32. Teixeira, C. Incorporating turbulence models into the lattice-Boltzmann method. *Int. J. Mod. Phys. C.* **09**, 1159–1175 (1998).
33. Chen, S. & Doolen, G. Lattice Boltzmann method for fluid flows. *Annu. Rev. Fluid Mech.* **30**, 329–364 (1998).
34. Ferrante, P., Roeck, W. D., Desmet, W. & Magnino, N. Back-to-back comparison of impedance measurement techniques applied to the characterization of aero-engine nacelle acoustic liners. *Appl. Acoust.* **105**, 129–142 (2016).
35. Murray, P., Ferrante, P. & Scofano, A. Manufacturing process and boundary layer influences on perforate liner impedance (2005).

36. Spillere, A. M. et al. Design of a single degree of freedom acoustic liner for a fan noise test rig. *Int. J. Aeroacoustics* **20**, 708–736 (2021).
37. Acoustics -" Determination of sound absorption coefficient and impedance in impedance tubes -" Part 2: Transfer-function method. Standard, International Organization for Standardization, Geneva, CH (1998).
38. Watson, W. R. & Jones, M. G. A comparative study of four impedance eduction methodologies using several test liners (2013).
39. Morse, P. & Ingard, U. *Theoretical Acoustics* (Princeton University Press, 1986), 1 edn.
40. Panton, R. & Miller, J. Resonant frequencies of cylindrical Helmholz resonators. *J. Acoust. Soc. Am.* **75**, 1533–1535 (1975).
41. Scarano, F., Lyu, B., Paduano, A. & Avallone, F. Filtering acoustic from hydrodynamic velocity using modal decomposition methods on an acoustic liner under grazing turbulent flow. *J. Sound Vib.* **625**, 119568 (2026).
42. Bonomo, L. A. et al. A comparison of impedance eduction test rigs with different flow profiles (2023).

Acknowledgements

The work of F. Avallone, A. Paduano and F. Scarano is co-funded by the European Union (ERC, LINING, 101075903). Views and opinions expressed are, however, those of the author(s) only and do not necessarily reflect those of the European Union or the European Research Council. Neither the European Union nor the granting authority can be held responsible for them. The work is partially supported by the AeroAcoustics Research Consortium (AARC), a government-industry partnership supporting pre-competitive research for aircraft noise reduction. L. Meirelles acknowledges scholarship funding from CNPq (168115/2023-9). The authors acknowledge Fundação CERTI (Brazil) for their contributions to the metrological aspects of this research. The authors thank D. Casalino for the discussions and suggestions about the numerical setup.

Author contributions

F.A. funding acquisition, conceptualization, numerical simulations and writing. A.K., data analysis, figures and writing. A.P., F.S. data analysis, figures, and reviewing. L.M. experiments and reviewing. J.C. funding acquisition and reviewing.

Competing interests

Author Francesco Avallone is an Editorial Board Member of NPJ Acoustics. Francesco Avallone was not involved in the journal's review of, or decisions related to, this manuscript. The other authors do not have a competing interest.

Additional information

Correspondence and requests for materials should be addressed to Francesco Avallone.

Reprints and permissions information is available at http://www.nature.com/reprints

Publisher's note Springer Nature remains neutral with regard to jurisdictional claims in published maps and institutional affiliations.

Open Access This article is licensed under a Creative Commons Attribution-NonCommercial-NoDerivatives 4.0 International License, which permits any non-commercial use, sharing, distribution and reproduction in any medium or format, as long as you give appropriate credit to the original author(s) and the source, provide a link to the Creative Commons licence, and indicate if you modified the licensed material. You do not have permission under this licence to share adapted material derived from this article or parts of it. The images or other third party material in this article are included in the article's Creative Commons licence, unless indicated otherwise in a credit line to the material. If material is not included in the article's Creative Commons licence and your intended use is not permitted by statutory regulation or exceeds the permitted use, you will need to obtain permission directly from the copyright holder. To view a copy of this licence, visit http://creativecommons.org/licenses/by-nc-nd/4.0/.

© The Author(s) 2026